

# Floquet-driven light transport in programmable photonic processors via discretized evolution of synthetic magnetic fields

Andrea Cataldo<sup>1,\*</sup>, Rohan Yadgirkar<sup>1</sup>, Ze-Sheng Xu<sup>1</sup>, Govind Krishna<sup>1</sup>, Ivan Khaymovich<sup>2</sup>, Val Zwiller<sup>1</sup>, Jun Gao<sup>1,\*</sup>, and Ali W. Elshaari<sup>1,\*</sup>

<sup>1</sup>Department of Applied Physics, KTH Royal Institute of Technology, Albanova University Centre, Roslagstullsbacken 21, 106 91 Stockholm, Sweden

<sup>2</sup>Nordita, KTH Royal Institute of Technology and Stockholm University, Hannes Alfvéns väg 11, 106 91 Stockholm, Sweden

\*Corresponding authors. Emails: [andreacl@kth.se](mailto:andreacl@kth.se), [junga@kth.se](mailto:junga@kth.se), [elshaari@kth.se](mailto:elshaari@kth.se)

## Abstract

Photons, unlike electrons, do not couple directly to magnetic fields, yet synthetic gauge fields can impart magnetic-like responses and enable directional transport. Discretized Floquet evolution provides a controlled route, where the time-ordered sequencing of non-commuting Hamiltonians imprints complex hopping phases and breaks time-reversal symmetry. However, stabilizing such driven dynamics and observing unambiguous signatures of these effects on a reconfigurable platform has remained challenging. Here we demonstrate synthetic gauge fields for light on a programmable photonic processor by implementing discretized Floquet drives that combine static and dynamic phases. The resulting dynamics exhibit chiral circulation that reverses under drive inversion, flux-controlled interference with high visibility,

and robust directional flow stabilized by optimizing the driving period. We further characterize the system using a first-harmonic phase as an order parameter, whose per-period winding number quantifies angular drift and reverses sign with the drive order. These results establish discretized Floquet evolution as a versatile framework for driven photonics, providing a programmable route to engineer gauge fields, stabilize driven phases, and probe winding-number signatures of chiral transport.

## 1. Introduction

Magnetic fields profoundly alter the behavior of charged particles by reshaping their energy spectrum. In two-dimensional electron systems, a perpendicular field condenses continuous bands into a hierarchy of discrete Landau levels, each separated by the cyclotron frequency and hosting a macroscopic degeneracy of states. This quantization underlies the quantum Hall effect, wherein the electrical conductance assumes precisely quantized values. The effect also produces chiral edge states, which are one-way electron channels along material boundaries that are topologically protected against backscattering from disorder [1, 2]. Photons propagate through such magnetic fields unchanged, their spectra unquantized, their transport unprotected. Remarkably, synthetic magnetic fields can induce analogous phenomena in photonic systems, thereby enabling magnetic-like responses and robust optical transport [3–5].

Several approaches have emerged to create these synthetic magnetic fields, broadly following two strategies: structural engineering and temporal modulation. Structural approaches exploit materials that break time-reversal symmetry or geometries that emulate gauge fields while preserving it. Magneto-optical materials provide non-reciprocal light propagation, wherein forward and backward traveling waves experience different phase shifts. Theoretical proposals [6, 7] and microwave demonstrations [8] have validated this approach. At optical frequencies, however, magneto-optical effects become vanishingly weak. Strain-engineered geometries constitute an alternative approach. Carefully designed lattice deformations create spatially varying coupling between optical modes, generating synthetic magnetic fields without magnetic materials. Theoretical work has established that such strain produces photonic Landau levels [9, 10]. These predictions have been confirmed through observations in strained honeycomb lattices [11] and silicon photonic crystals [12, 13]. Temporal approaches, in contrast, can break reciprocity through harmonic mod-

ulation of optical properties. Such modulation targets either the coupling between resonators [14] or refractive index within resonators [15]. Diverse platforms have realized this principle, from optomechanical systems [16] to integrated electro-optic devices [17, 18].

In this work, we demonstrate a photonic simulator of synthetic magnetic fields based on discrete-time evolution. The simulator is implemented on a reconfigurable Mach-Zehnder interferometer (MZI) mesh, which supports arbitrary linear optical transformations [19, 20] and has enabled applications in quantum information processing [21–24], neuromorphic computing [25, 26], and signal processing [27, 28]. We use a Floquet drive in which each period is divided into unitary substeps that sequentially activate selected waveguide pairs on the MZI mesh while other couplings are held off. The time-ordered product of these steps induces complex hopping phases for photons, realizing a synthetic magnetic flux. Because the substeps do not commute, the evolution depends on their order, which breaks time-reversal symmetry. This programmability allows a single photonic processor to investigate various driven phenomena without separate fabrications by simply adjusting control signals [29, 30], building on recent implementations of programmable lattices in integrated photonic meshes [31–34]. Leveraging this versatility, we implement three-, four-, and seven-site lattice configurations. Our measurements reveal how each geometry produces distinct magnetic signatures, with the three-site system establishing the fundamental mechanism, the four-site system revealing flux interference, and the seven-site system demonstrating directional photon transport in complex systems.

## 2. Methods

### 2.1. Theoretical framework

Our approach utilizes discretized Floquet dynamics to induce synthetic gauge fields for photons. By subjecting the lattice to a time-ordered sequence of non-commuting unitary operations, we break time-reversal symmetry and imprint a path-dependent geometric phase on the photon transport.

Consider a programmable lattice governed by a periodic modulation cycle  $T$ . We partition the evolution into a sequence of discrete unitary operations  $U_k$  (Fig. 1a,b), where each step activates a specific subset of couplings for a duration  $T/3$  (Fig. 1c). While the instantaneous Hamiltonian

at any step could be reciprocal, the non-commutativity of the sequence ( $[U_k, U_{k'}] \neq 0$ ) renders the total Floquet operator  $U_F(T)$  distinct from its time-reversed counterpart. Physically, this temporal ordering allows us to define distinct clockwise (CW) and counter-clockwise (CCW) evolution operators (see section S1).

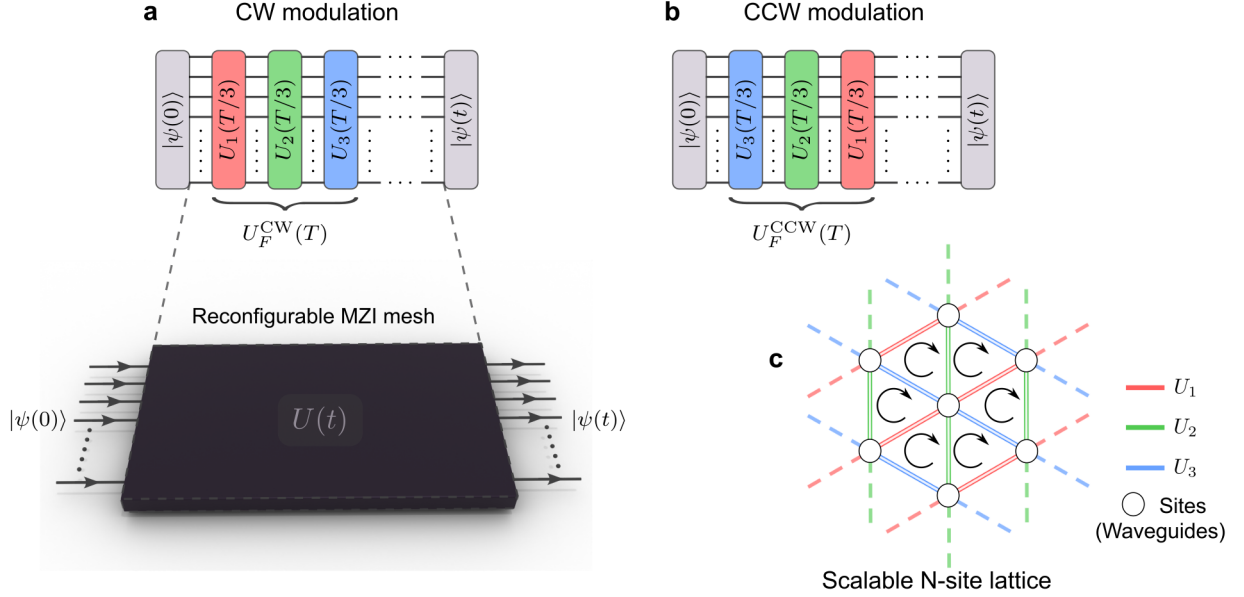


**Fig. 1. Discretized Floquet evolution on a programmable photonic processor.** A state  $|\psi(0)\rangle$  injected on the left bus enters a programmable photonic processor consisting of a reconfigurable MZI mesh (black box) that implements the time-evolution operator  $U(t)$  on  $N$  spatial waveguide modes, yielding  $|\psi(t)\rangle = U(t)|\psi(0)\rangle$  at the right bus. **a**, CW drive: one period  $T$  is decomposed into three sequential substeps  $U_1(T/3)$  (red),  $U_2(T/3)$  (green), and  $U_3(T/3)$  (blue). These time-ordered operations constitute the Floquet operator  $U_F^{CW}(T) = U_3U_2U_1$ . Dashed guide lines indicate that this schedule is programmed onto the chip; horizontal dots indicate repetition over successive periods. At intermediate times (e.g.,  $t = T/3$ ), only the substep executed up to that moment has acted. **b**, CCW drive obtained by reversing the order of the substeps, giving  $U_F^{CCW}(T) = U_1U_2U_3$ . **c**, Scalable  $N$ -site lattice representation. Lattice sites (white circles) map to physical waveguides, while solid colored bonds represent the tunable couplings realized by the MZI mesh active in the respective substeps (colors match panels a–b); dashed bond extensions indicate tiling to larger lattices. Curved arrows highlight the induced chiral circulation in each triangular plaquette, illustrating how the programmed drive order generates a synthetic magnetic flux.

To capture the complete transient dynamics of this driven system, we define the total time-evolution operator  $U(t)$ . For an arbitrary time  $t = nT + \delta t$  (where  $n$  is the number of completed cycles and  $\delta t$  is the remainder,  $0 \leq \delta t < T$ ), the evolution is given by:

$$U(t) = U_{\text{partial}}(\delta t)[U_F(T)]^n, \quad (1)$$

where  $[U_F(T)]^n$  describe the stroboscopic dynamics over full cycles, and  $U_{\text{partial}}(\delta t)$  accounts for the residual intra-period evolution.

Stroboscopically, the system behaves as if governed by a time-independent effective Hamiltonian with complex couplings. The time-ordered drive ensures that a photon hopping between sites acquires a geometric phase analogous to the Aharonov-Bohm phase. The accumulation of these phases (e.g. around a closed triangular plaquette) generates a synthetic magnetic flux  $\Phi_{\text{mod}}$ . This flux relates formally to a synthetic vector potential  $\mathbf{A}$ , where the phase  $\phi$  acquired along a link is given by the line integral  $\phi = \int \mathbf{A} \cdot d\mathbf{l}$ . Furthermore, we can augment this geometric phase by imprinting programmable static phases  $\Phi_{\text{static}}$  onto the lattice bonds, allowing the total accumulated flux  $\Phi_{\text{total}} = \Phi_{\text{mod}} + \Phi_{\text{static}}$  to be fully tunable (see section S1).

## 2.2. Experimental platform

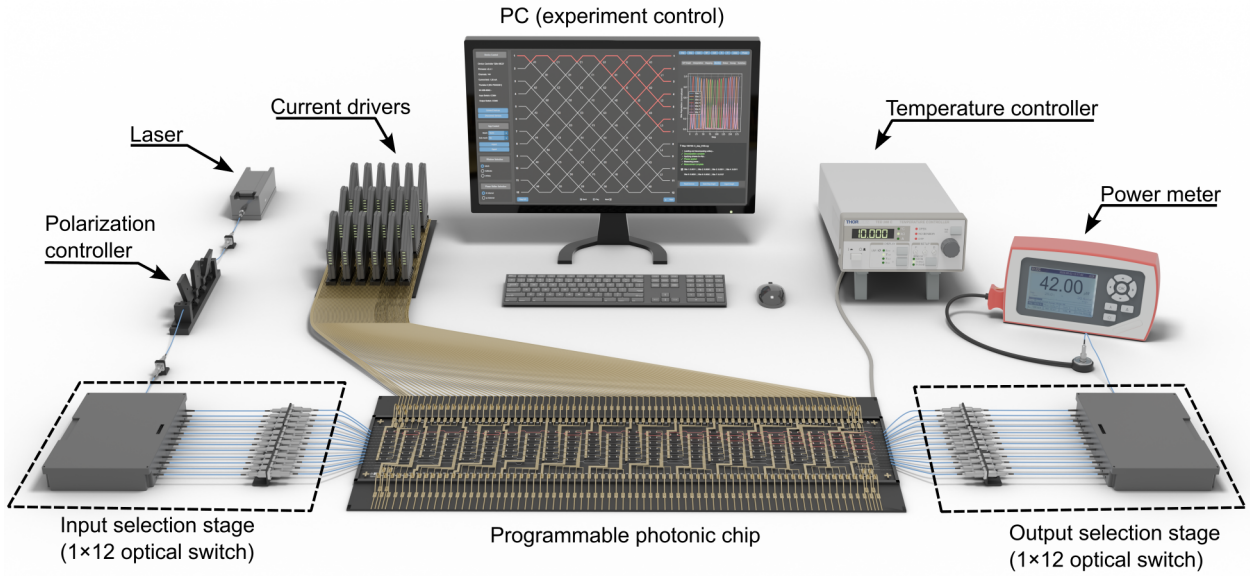


**Fig. 2. Experimental setup.** Coherent light at 1550 nm from a pulsed diode laser passes through a polarization controller set for TE polarization and is directed to the common port of a  $1 \times 12$  MEMS optical switch. The switch can be programmed to route the light to any of its twelve multiplexed ports. These ports couple via edge couplers to the corresponding input waveguides of a 12-mode programmable photonic chip, thereby selecting the input. The chip consists of a reconfigurable MZI mesh driven by multichannel current drivers. Light at the chip output is coupled via edge couplers into a second switch operated in reverse; its common port is connected to an optical power meter. Control and acquisition are handled by a PC, which commands the switches, sets the heater currents to realize the unitaries, and logs readings from the power meter. A thermoelectric cooler beneath the chip, regulated by a PID temperature controller, maintains a fixed room-temperature setpoint.

The experimental platform (Fig. 2) was based on a 12-mode photonic processor. Here, the 12 modes represent independent spatial waveguide paths that constitute the Hilbert space of the system, where each waveguide acts as a discrete site in our programmed synthetic geometry.

The processor integrates 264 active elements, consisting of a mesh of thermally tuned MZIs and multimode interferometers (MMIs). Deep trenches were included around the MZIs to suppress thermal crosstalk between neighboring phase shifters.

A pulsed diode laser driver provided the coherent light source at 1550 nm. Light was routed to individual chip inputs via a MEMS fiber optical switch optimized for TE polarization. Output signals were collected through a second identical switch connected to a high-sensitivity optical power meter with a germanium photodiode sensor. A PC coordinated all instruments to provide full automation. Phase relationships were preserved by stabilizing the chip temperature using a thermoelectric cooler and PID controller. Detailed technical specifications of the experimental platform are provided in sections S2 to S3.

### **2.3. Lattice realization and driving protocols**

The programmable photonic chip allowed us to implement three distinct lattice configurations. We first realized a three-site triangular lattice whose single closed loop allowed clear interpretation of directional effects when driving CW and CCW, isolating the non-commuting operations that break time-reversal symmetry. We then programmed a four-site lattice consisting of two coupled triangular lattices with independent phase control. The shared vertices where pathways converge provided observation points for interference effects. Finally, we configured a seven-site hexagonal lattice to test synthetic magnetic fields in multi-loop geometries. Six perimeter sites surrounding a central node formed a network of interconnected triangular plaquettes, revealing whether directional transport persists in complex systems.

Operating conditions varied across lattice configurations based on their specific requirements. For coherent population transfer in the three-site and four-site systems, we set coupling strengths and evolution times to achieve Rabi  $\pi$ -pulses. This operating point is robust to perturbations in a broad range, given by a finite gap in the corresponding spectrum of the three-site Floquet operator, so the dynamics are tolerant to small period errors as elucidated in the Results (Section 3.3). While the triangular lattice experiments tested both modulation sequences to establish chirality, the four-site system used only CW driving to focus solely on the interference effects. The seven-site system required a different regime where Rabi pulses are not applicable, so we selected the modulation period by maximizing the minimal quasi-energy gap of the Floquet operator, which

yields a stable evolution and robust directional flow. As in the 3-site case, testing both modulation sequences would confirm the presence of the synthetic magnetic field signatures.

## 2.4. Unitary implementation

We realized the evolution operators by decomposing the target unitary  $U(t)$  into a sequence of local operations on the mesh. Each MZI implements a  $SU(2)$  transformation, parameterized by two independent phase degrees of freedom. To map the theoretical models onto the device, we defined the  $n$  lattice sites as a subspace of the available spatial modes. The target  $n \times n$  operator was embedded into the processor's full Hilbert space by decoupling the inactive waveguides, ensuring the evolution remained confined to the synthetic lattice.

We then employed the Clements decomposition [20] to factorize this high-dimensional unitary into a deterministic arrangement of local phase shifts for the mesh. To ensure high-fidelity control, these target phases were mapped to heater currents using a calibrated nonlinear response model that compensates for fabrication variances. Further details regarding the unitary implementation are found in sections S4 to S6.

## 2.5. Data acquisition and analysis

To resolve the transient population dynamics, we applied the unitary evolution operators incrementally. Each modulation period  $T$  was divided into 60 discretized steps (20 per subprocess). For a given time step  $t$ , the cumulative operator  $U(t)$  was decomposed into phase configurations applied to the MZI mesh. The system was initialized in state  $|1\rangle$  for the three-site and seven-site lattices, while the four-site lattice utilized a symmetric superposition  $(|1\rangle + |3\rangle)/\sqrt{2}$  prepared via the first layers of the mesh. At each step, output powers were measured across all active waveguides using an optical power meter. To account for fiber-to-chip coupling variations, the raw power readings were normalized to the total detected power at that time step. We estimated experimental uncertainties by propagating a  $\pm 3\%$  relative uncertainty through the normalization procedure (see section S7).

### 3. Results

#### 3.1. Minimal geometry for synthetic magnetic fields

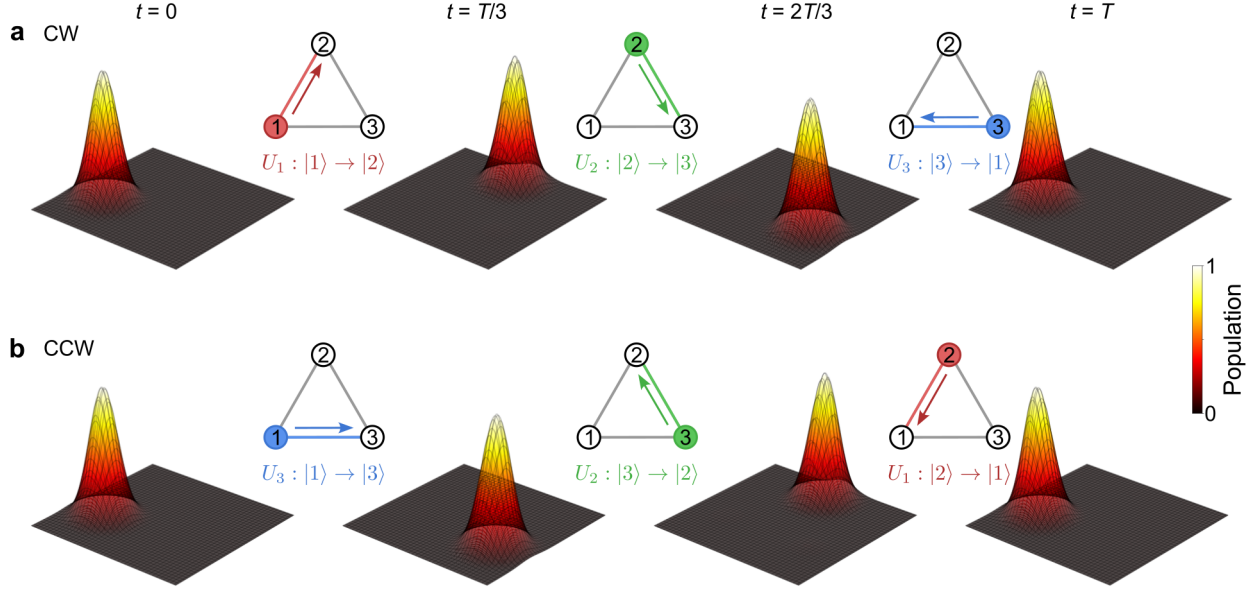


**Fig. 3. Chiral photon transport in a three-site plaquette.** Each row shows four snapshots of the system’s state, taken at the switching boundaries  $t = 0, T/3, 2T/3$  and  $T$ . For every snapshot, the colored surface represents the experimental normalized population, rendered as a single smooth surface by summing three Gaussian peaks centered at the lattice sites. The black wireframe overlays the simulated population. In the triangular schematics, a colored bond marks the active substep, with  $U_1(T/3)$  red,  $U_2(T/3)$  green, and  $U_3(T/3)$  blue. The arrow direction indicates the transport directionality, and gray bonds are off. **a**, For clockwise (CW) modulation, the population transfers sequentially along the path  $1 \rightarrow 2 \rightarrow 3 \rightarrow 1$ . **b**, For counter-clockwise (CCW) modulation, the sequence reverses to  $1 \rightarrow 3 \rightarrow 2 \rightarrow 1$ . The close surface-wireframe overlap indicates excellent agreement. Reversing the drive clearly reverses the circulation.

Fig. 3 presents snapshots of the population dynamics for a system initialized with unit population at site 1. The evolution spans one complete modulation period  $T$ . Under CW modulation (Fig. 3a), the time-ordered sequence defined in Fig. 1a drives coherent population transfer along the path  $1 \rightarrow 2 \rightarrow 3 \rightarrow 1$ . The system operates with Rabi  $\pi$ -pulses ( $JT/3 = \pi/2$ ) to ensure complete transfer between coupled sites. Simulation results reveal near-perfect sequential transfer at the expected times. Experimental measurements yield target-site populations of  $99.05 \pm 0.04\%$ ,  $99.09 \pm 0.04\%$ , and  $99.70 \pm 0.01\%$ .

CCW modulation (Fig. 3b) implements the reversed evolution sequence, driving population along  $1 \rightarrow 3 \rightarrow 2 \rightarrow 1$ . Both simulation and experiment demonstrate comparable efficiency,

with measured populations of  $99.57 \pm 0.02\%$ ,  $98.47 \pm 0.06\%$ , and  $99.78 \pm 0.01\%$ . The opposite circulation patterns generate artificial magnetic fluxes of opposite signs, directly confirming time-reversal symmetry breaking in our programmable platform.

We also note that the observed circulation depends on the choice of initialization site. Starting from site 1 produces one-period CW/CCW cycles as demonstrated. If instead the system is prepared on site 2 or 3, the population moves only every other substep, so the effective circulation appears reversed and closes only after two periods. Thus, on average the magnetic field is zero, but it depends on both site location and the phase of the drive.

### 3.2. Flux-steered interferometry in a two-plaquette lattice

The next step extends the single triangle to a pair of triangular plaquettes that share an edge, forming a two-path interferometer configuration. Both plaquettes are driven by the CW time-ordered sequence with period  $T = 3\pi/(2J)$ . Static phases are programmed on the outer bonds to set loop phases  $\Phi_A$  and  $\Phi_B$  around plaquettes A and B. Because the modulation-induced phase  $\Phi_{\text{mod}}$  is common to both loops, the relevant quantity that steers interference at the shared vertices is the synthetic flux difference  $\Delta\Phi \equiv \Phi_A - \Phi_B$ . This cancellation of the modulation phase allows us to isolate the static contribution.

Fig. 4 presents the implementation and readout of this interferometer. Panel a shows the lattice schematic (sites 1-4) where bonds are color-coded to the three substeps of the CW drive ( $U_1$  red,  $U_2$  green on the shared edge, and  $U_3$  blue). The circular arrows label the net loop phases  $\Phi_A$  and  $\Phi_B$  around the left and right triangles; individual bond phases are not depicted. The input is prepared in the symmetric superposition  $(|1\rangle + |3\rangle)/\sqrt{2}$  so that amplitudes launch into both loops. During one drive period  $T$ , the CW sequence routes these amplitudes to the shared sites 2 and 4 where they interfere. With this initial state, reversing the drive order yields indistinguishable populations at the shared sites, so the protocol's time-reversal symmetry breaking is obscured in this configuration. Using a different input, such as adding a relative phase between  $|1\rangle$  and  $|3\rangle$ , would reveal the driving direction. Here we focus on the interferometric response.

The resulting interference is shown in panel b as the simulated mid-period populations  $P_2(T/2)$  and  $P_4(T/2)$  as  $\Delta\Phi$  is swept. The two traces are complementary and cross at  $\Delta\Phi = 0$ , where the populations are balanced. This follows from a two-path picture. During  $U_2$  the

fields at the shared sites are coherent sums of the amplitudes from the two plaquettes that differ only by the programmed flux difference. With the phase origin chosen so that  $\Delta\Phi = 0$  yields equal populations, the dependence is consistent with  $P_{2,4}(T/2) = \frac{1}{2}[1 \pm V \sin(\Delta\Phi/2)]$ , where  $0 \leq V \leq 1$  is the visibility, the upper sign corresponds to site 2, and the lower to site 4. This form explains the smooth S-shaped exchange of population and the complementarity  $P_2 + P_4 = 1$ .

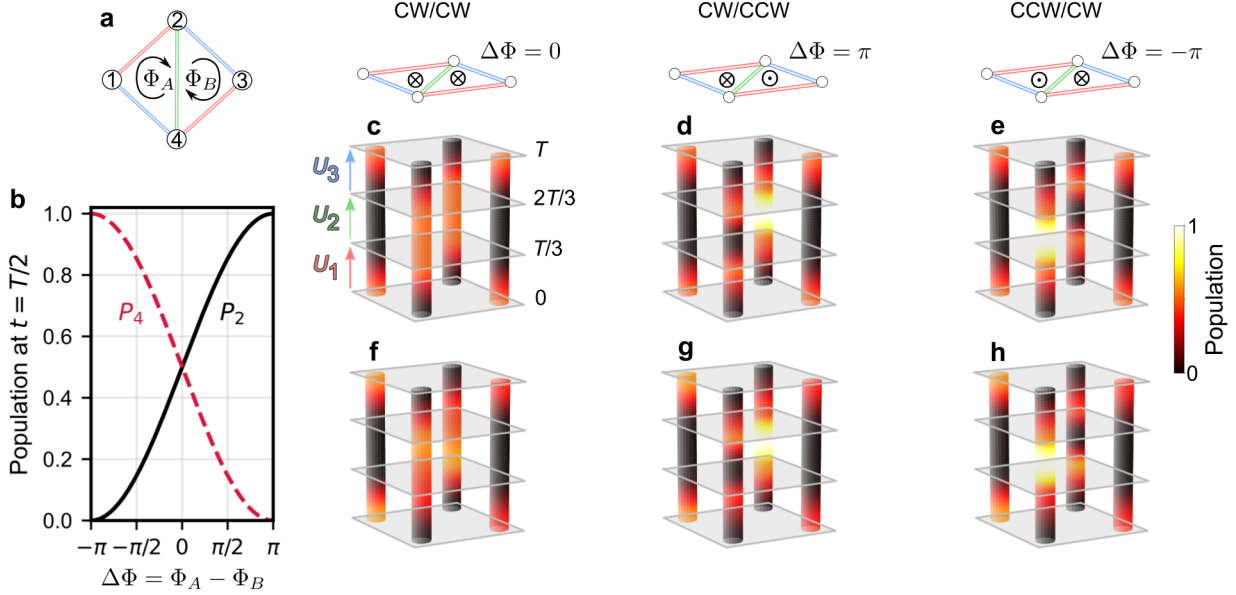


**Fig. 4. Flux-tuned interference in a four-site lattice.** **a**, Schematic of two triangles A and B with a shared edge (green), driven by the CW sequence  $U_1$  (red),  $U_2$  (green), and  $U_3$  (blue). Triangles A and B have loop fluxes  $\Phi_A$  and  $\Phi_B$ , respectively. Interference at the shared vertices (sites 2 and 4) is governed by their flux difference  $\Delta\Phi \equiv \Phi_A - \Phi_B$ . The initial state is  $(|1\rangle + |3\rangle)/\sqrt{2}$ , launching light into both loops. **b**, Simulated mid-period ( $t = T/2$ ) populations  $P_2$  (black) and  $P_4$  (red, dashed) versus  $\Delta\Phi$ ; the traces are complementary and cross at  $\Delta\Phi = 0$ . **c-e**, Simulated dynamics over one period  $t = T$  for  $\Delta\Phi = 0$  (CW/CW),  $+\pi$  (CW/CCW), and  $-\pi$  (CCW/CW). Horizontal planes mark  $t = 0, T/3, 2T/3, T$  and the colored labels indicate the active substep  $U_1, U_2, U_3$  between planes. Insets use  $\otimes/\odot$  to denote flux into/out of the triangle plane (drawn above population columns). **f-h**, Measured dynamics for the same settings, showing balanced splitting at  $\Delta\Phi = 0$ , constructive interference at site 2 for  $+\pi$ , and at site 4 for  $-\pi$ , in agreement with simulations. In the latter two cases, destructive interference suppresses the green link, so the effective dynamics proceed primarily through the red and blue couplings. Color scale indicates normalized population.

Panels c-e display simulated population dynamics for three representative settings of  $\Delta\Phi$ . For  $\Delta\Phi = 0$  (CW/CW in the relative sense), the amplitudes from the two loops arrive in phase, distributing populations equally at sites 2 and 4 at the mid-period. Shifting to  $\Delta\Phi = +\pi$  (CW/CCW) reverses the relative sign of one path, so that constructive interference occurs at site 2 while destructive interference suppresses site 4. Reversing the sign to  $\Delta\Phi = -\pi$  flips the pattern, brightening site 4 and dimming site 2.

Panels f-h present the measurements. As  $\Delta\Phi$  is tuned from 0 to  $+\pi$  and then to  $-\pi$ , the population shifts between the two shared sites in agreement with the simulations. At the mid-period, the balanced case ( $\Delta\Phi = 0$ ) yields  $P_2 = 50.29 \pm 1.05\%$  and  $P_4 = 48.73 \pm 1.05\%$ . A relative shift of  $+\pi$  favors site 2 ( $96.77 \pm 0.11\%$ ) while suppressing site 4 ( $2.03 \pm 0.08\%$ ), and reversing the sign inverts the distribution, with site 4 at  $98.28 \pm 0.06\%$  and site 2 at  $0.73 \pm 0.03\%$ .

### 3.3. Directional transport in a multi-plaquette hexagonal lattice

We now scale to a geometry where intertwined loops come together in a seven-site hexagon surrounding a central site. In the three-site and four-site lattices each step of the drive couples only two sites, so the evolution follows simple two-level dynamics with complete transfer via Rabi  $\pi$ -pulses. This clear condition no longer applies in lattices where a driving step may couple more than two sites, which breaks the isolated two-level picture and makes the effective Floquet Hamiltonian long-ranged. We therefore identify stable operating points by examining the quasi-energy spectrum of the Floquet operator  $U_F$ . Its eigenvalues take the form  $\lambda_k = e^{-i\varepsilon_k T}$ , where the quasi-energies satisfy  $0 \leq \varepsilon_k < 2\pi/T$ . The stability of the dynamics is set by the separation between the quasi-energies, defined as the minimal splitting  $\Delta\varepsilon_{\min} = \min_{i \neq j} |\varepsilon_i - \varepsilon_j|$ , which quantifies the smallest gap in the spectrum (distance measured mod  $2\pi/T$  on a circle).

In any physical implementation the ideal operator  $U_F(T)$  is subject to small, random perturbations in control parameters (e.g. heater currents), leading to an implemented operator  $U_{\text{actual}}(T) = U_F(T) + \delta U$ , where  $\delta U$  is a random matrix representing the integrated effect of experimental imperfections over one period. A small gap ( $\Delta\varepsilon_{\min} \rightarrow 0$ ) indicates a near-degeneracy where the system's final state becomes highly sensitive to  $\delta U$ , causing the states to mix unpredictably. A larger gap corresponds to a more stable, well-separated evolution, which ensures the evolution is robust against such perturbations. Our strategy is therefore to find the optimal period,  $T_{\text{opt}}$ , that maximizes this gap:

$$T_{\text{opt}} = \arg \max_T [\Delta\varepsilon_{\min}(T)]. \quad (2)$$

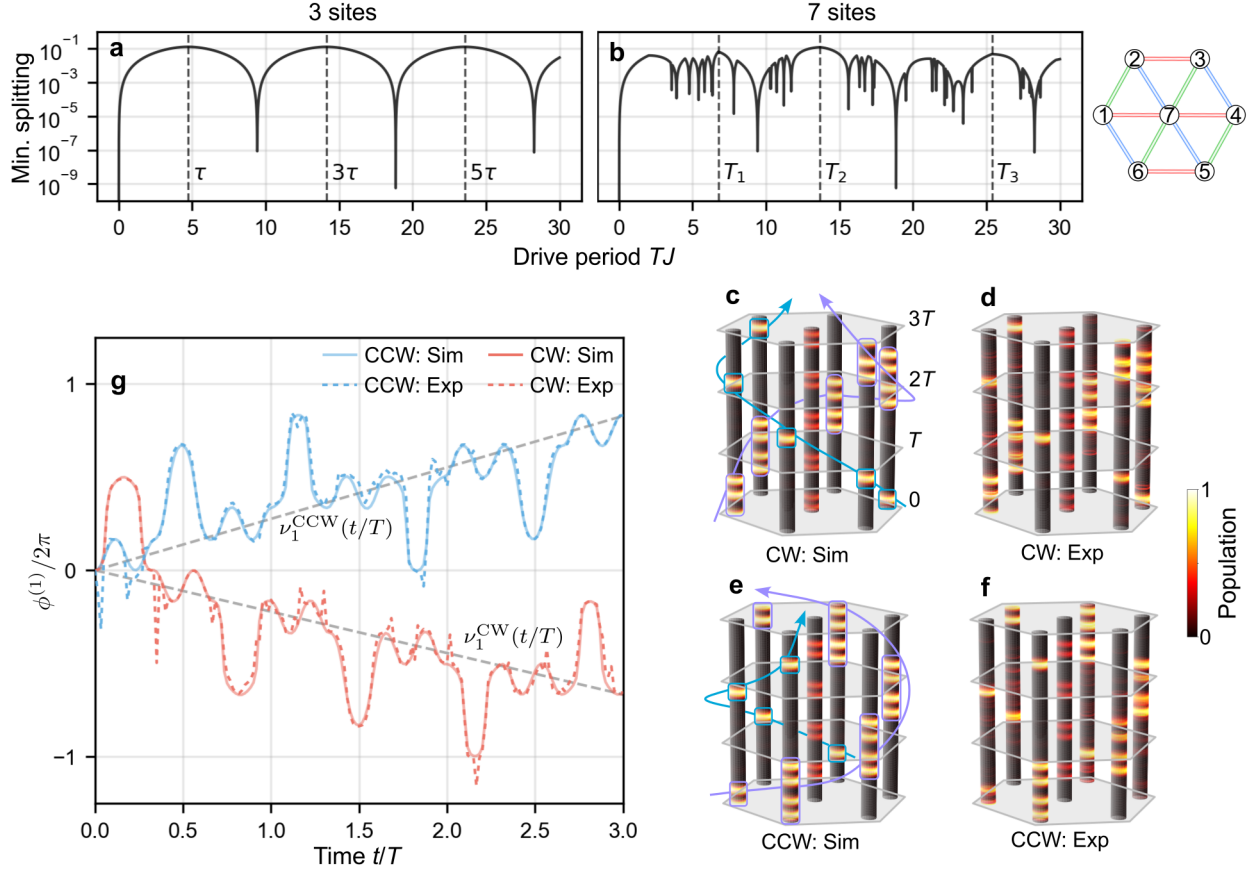


**Fig. 5. Floquet-period optimization and directional transport in a seven-site hexagon.** Top-right: schematic of the lattice with color-coded bonds (red/green/blue for  $U_1/U_2/U_3$ ). The system is initialized in state  $|1\rangle$ . **a**, Minimal quasi-energy splitting  $\Delta\varepsilon_{\min}$  of the three-site Floquet operator  $U_F(T)$  versus drive period  $T$  (dimensionless;  $J = \hbar = 1$ ). Peaks at  $\tau$ ,  $3\tau$ ,  $5\tau$  mark the Rabi  $\pi$  condition and its odd multiples with the maximum splitting reaching  $\Delta\varepsilon_{\min} = 0.125$ . The dips indicate near-degeneracy of quasi-energies. **b**, In the seven-site case, operating points are identified at  $T_1 = 6.7574$ ,  $T_2 = 13.6647$  (used in sim/exp,  $\Delta\varepsilon_{\min} = 0.119$ ), and  $T_3 = 25.3791$ . **c,d**, CW modulation: simulated and experimental population dynamics over three driving periods ( $t = 3T$ ). Oscillatory exchanges are observed within each substep with an overall CW circulation. Violet boxes mark the multi-peak packet and cyan boxes the single-peak packet, with an overlaid arrow indicating the trajectory; these two contributions form a superposition and both advance in the CW sense. **e,f**, For CCW modulation, the circulation reverses: the same guides show the multi-peak and single-peak packets advancing CCW. **g**, First harmonic Fourier phase  $\phi^{(1)}/2\pi$  from the measured and simulated dynamics. Solid (sim) and dashed (exp) are overlaid. Gray guide lines with slopes  $\nu_1^{\text{CCW}} = 0.276$  and  $\nu_1^{\text{CW}} = -0.222$  indicate the extracted per-period winding numbers. Traces show opposite overall trends for CW (red) versus CCW (blue), consistent with broken time-reversal symmetry. Movies of evolutions are provided in the Supplementary Materials.

To validate the period-selection procedure, we first applied it to the 3-site lattice. The results, shown in Fig. 5a, reveal a periodic spectrum of stability peaks. Notably, one of these peaks at  $T = 4.7109$  coincides with the familiar  $\pi$ -pulse condition, while the subsequent peaks represent its odd multiples, where a complete state transfer also occurs. This confirms our method correctly identifies the entire family of known coherent evolution points, each corresponding to a

non-degenerate system with a minimal splitting of  $\Delta\varepsilon_{\min} = 0.125$ .

We then evaluated the seven-site hexagon (Fig. 5b). Although more complex, the system retains features of the 3-site lattice, including the shared near-degeneracy locations. An optimal peak  $T_{\text{opt}} = 13.6647$  was selected for the experiment, which occurs near a stability peak of its underlying 3-site building block  $T = 14.1388$ . Consequently, the seven quasi-energies arrange themselves into a near-uniform, maximally gapped configuration ( $\Delta\varepsilon_{\min} = 0.119$ ).

The seven-site hexagonal lattice presents qualitatively different behavior from our minimal configurations. Fig. 5(c-f) shows population dynamics over three modulation periods  $t = 3T$ , demonstrating oscillatory exchange between coupled sites superimposed on global directional flow. These oscillations migrate around the hexagon with each Hamiltonian switch, producing a clear rotating pattern that follows the modulation direction throughout the evolution. The drive produces sequential site occupations with high population transfer at various stages, while the central site (7) acts mainly as a transient hub and remains only weakly populated overall. The clockwise case is shown in Fig. 5(c,d) and the counterclockwise case in Fig. 5(e,f), where reversing the drive order flips the direction of the rotating pattern. Extended  $9T$  dynamics showing more than one full rotation are provided in section S8.

As a complementary view of the transport, Fig. 5g shows the first-harmonic Fourier phase extracted from the measured and simulated populations. Assign each site an azimuthal angle  $\theta_k$  according to the lattice geometry (with the central site taken as  $\theta_7 = 0$ ), and the complex first-harmonic is formed as  $C^{(1)}(t) = \sum_{k=1}^7 P_k(t) e^{i\theta_k}$ , where  $P_k(t)$  is the population at site  $k$ . Its phase  $\phi^{(1)}(t) = \arg[C^{(1)}(t)]$  provides a measure of the net angular drift and is expected to have an overall linear growth. Expressed in cycles (i.e.,  $\phi^{(1)}/2\pi$ ), the phase drifts nearly linearly over the periods; the slope's sign sets the transport direction, and small kinks appear when population transiently occupies the central site, pulling  $C^{(1)}(t)$  toward  $\theta = 0$ . We quantify this drift by an empirical per-period winding number,  $\nu_1 \equiv \frac{1}{2\pi} \frac{d\phi^{(1)}}{d(t/T)}$ , i.e., the slope of  $\phi^{(1)}/2\pi$  versus  $t/T$ . From Fig. 5g we obtain  $\nu_1^{\text{CW}} = -0.222$  and  $\nu_1^{\text{CCW}} = +0.276$ , with the sign reversing under drive inversion. The experimental traces follow closely (correlation  $r = 0.989$  for CW;  $r = 0.985$  for CCW). While the seven-site, open system does not enforce quantization, the nonzero and sign-robust  $\nu_1$  is consistent with a nontrivial per-period phase winding and the observed chiral transport.

## 4. Conclusion

In this work, we have demonstrated that discretized Floquet evolution on a programmable photonic processor provides a powerful and highly flexible method for generating synthetic gauge fields. By systematically breaking time-reversal symmetry with time-ordered coupling sequences, we validated the core principles of this approach, progressing from the demonstration of fundamental chiral transport in a single plaquette to coherent, flux-controlled routing in an interferometric geometry, and finally to directional transport in a complex multi-loop lattice. This technique moves beyond static, fabrication-defined implementations by offering a fully programmable route to engineer complex Hamiltonians and explore a wide range of driven phenomena on a single chip.

## References

- [1] D. J. Thouless, M. Kohmoto, M. P. Nightingale, and M. den Nijs, “Quantized hall conductance in a two-dimensional periodic potential,” *Phys. Rev. Lett.*, vol. 49, pp. 405–408, Aug 1982.
- [2] B. I. Halperin, “Quantized hall conductance, current-carrying edge states, and the existence of extended states in a two-dimensional disordered potential,” *Phys. Rev. B*, vol. 25, pp. 2185–2190, Feb 1982.
- [3] R. O. Umucalılar and I. Carusotto, “Artificial gauge field for photons in coupled cavity arrays,” *Physical Review A*, vol. 84, no. 4, Oct. 2011.
- [4] K. Fang, Z. Yu, and S. Fan, “Photonic aharonov-bohm effect based on dynamic modulation,” *Phys. Rev. Lett.*, vol. 108, p. 153901, Apr 2012.
- [5] M. Hafezi, S. Mittal, J. Fan, A. Migdall, and J. M. Taylor, “Imaging topological edge states in silicon photonics,” *Nature Photonics*, vol. 7, no. 12, p. 1001–1005, Oct. 2013.
- [6] F. D. M. Haldane and S. Raghu, “Possible realization of directional optical waveguides in photonic crystals with broken time-reversal symmetry,” *Phys. Rev. Lett.*, vol. 100, p. 013904, Jan 2008.

- [7] S. Raghu and F. D. M. Haldane, “Analogues of quantum-hall-effect edge states in photonic crystals,” *Phys. Rev. A*, vol. 78, p. 033834, Sep 2008.
- [8] Z. Wang, Y. Chong, J. D. Joannopoulos, and M. Soljačić, “Observation of unidirectional backscattering-immune topological electromagnetic states,” *Nature*, vol. 461, no. 7265, pp. 772–775, 2009.
- [9] M. C. Rechtsman, J. M. Zeuner, A. Tünnermann, S. Nolte, M. Segev, and A. Szameit, “Strain-induced pseudomagnetic field and photonic Landau levels in dielectric structures,” *Nature Photonics*, vol. 7, no. 2, pp. 153–158, 2013.
- [10] J. Guglielmon, M. C. Rechtsman, and M. I. Weinstein, “Landau levels in strained two-dimensional photonic crystals,” *Phys. Rev. A*, vol. 103, p. 013505, Jan 2021.
- [11] O. Jamadi, E. Rozas, G. Salerno, M. Milićević, T. Ozawa, I. Sagnes, A. Lemaître, L. Le Gratiet, A. Harouri, I. Carusotto, J. Bloch, and A. Amo, “Direct observation of photonic Landau levels and helical edge states in strained honeycomb lattices,” *Light: Science & Applications*, vol. 9, no. 1, p. 144, 2020.
- [12] R. Barczyk, L. Kuipers, and E. Verhagen, “Observation of Landau levels and chiral edge states in photonic crystals through pseudomagnetic fields induced by synthetic strain,” *Nature Photonics*, vol. 18, no. 6, pp. 574–579, 2024.
- [13] M. Barsukova, F. Gris , Z. Zhang, S. Vaidya, J. Guglielmon, M. I. Weinstein, L. He, B. Zhen, R. McEntaffer, and M. C. Rechtsman, “Direct observation of Landau levels in silicon photonic crystals,” *Nature Photonics*, vol. 18, no. 6, pp. 580–585, 2024.
- [14] K. Fang, Z. Yu, and S. Fan, “Realizing effective magnetic field for photons by controlling the phase of dynamic modulation,” *Nature Photonics*, vol. 6, no. 11, pp. 782–787, 11 2012.
- [15] L. D. Tzuang, K. Fang, P. Nussenzveig, S. Fan, and M. Lipson, “Non-reciprocal phase shift induced by an effective magnetic flux for light,” *Nature Photonics*, vol. 8, no. 9, pp. 701–705, 9 2014.

- [16] M. Schmidt, S. Kessler, V. Peano, O. Painter, and F. Marquardt, “Optomechanical creation of magnetic fields for photons on a lattice,” *Optica*, vol. 2, no. 7, pp. 635–641, Jul 2015.
- [17] A. Dutt, Q. Lin, L. Yuan, M. Minkov, M. Xiao, and S. Fan, “A single photonic cavity with two independent physical synthetic dimensions,” *Science*, vol. 367, no. 6473, pp. 59–64, 2020.
- [18] H. X. Dinh, A. Balčytis, T. Ozawa, Y. Ota, G. Ren, T. Baba, S. Iwamoto, A. Mitchell, and T. G. Nguyen, “Reconfigurable synthetic dimension frequency lattices in an integrated lithium niobate ring cavity,” *Communications Physics*, vol. 7, no. 1, p. 185, 6 2024.
- [19] M. Reck, A. Zeilinger, H. J. Bernstein, and P. Bertani, “Experimental realization of any discrete unitary operator,” *Phys. Rev. Lett.*, vol. 73, pp. 58–61, Jul 1994.
- [20] W. R. Clements, P. C. Humphreys, B. J. Metcalf, W. S. Kolthammer, and I. A. Walmsley, “Optimal design for universal multiport interferometers,” *Optica*, vol. 3, no. 12, pp. 1460–1465, Dec 2016.
- [21] J. Carolan, C. Harrold, C. Sparrow, E. Martín-López, N. J. Russell, J. W. Silverstone, P. J. Shadbolt, N. Matsuda, M. Oguma, M. Itoh *et al.*, “Universal linear optics,” *Science*, vol. 349, no. 6249, pp. 711–716, 2015.
- [22] X. Qiang, X. Zhou, J. Wang, C. M. Wilkes, T. Loke, S. O’Gara, L. Kling, G. D. Marshall, R. Santagati, T. C. Ralph, J. B. Wang, J. L. O’Brien, M. G. Thompson, and J. C. F. Matthews, “Large-scale silicon quantum photonics implementing arbitrary two-qubit processing,” *Nature Photonics*, vol. 12, no. 9, pp. 534–539, 9 2018.
- [23] S. Paesani, Y. Ding, R. Santagati, L. Chakhmakhchyan, C. Vigliar, K. Rottwitt, L. K. Oxenløwe, J. Wang, M. G. Thompson, and A. Laing, “Generation and sampling of quantum states of light in a silicon chip,” *Nature Physics*, vol. 15, no. 9, pp. 925–929, 9 2019.
- [24] J. Wang, F. Sciarrino, A. Laing, and M. G. Thompson, “Integrated photonic quantum technologies,” *Nature Photonics*, vol. 14, no. 5, pp. 273–284, 5 2020.
- [25] Y. Shen, N. C. Harris, S. Skirlo, M. Prabhu, T. Baehr-Jones, M. Hochberg, X. Sun, S. Zhao, H. Larochelle, D. Englund, and M. Soljačić, “Deep learning with coherent nanophotonic circuits,” *Nature Photonics*, vol. 11, no. 7, pp. 441–446, 7 2017.

- [26] B. J. Shastri, A. N. Tait, T. Ferreira de Lima, W. H. P. Pernice, H. Bhaskaran, C. D. Wright, and P. R. Prucnal, “Photonics for artificial intelligence and neuromorphic computing,” *Nature Photonics*, vol. 15, no. 2, pp. 102–114, 2 2021.
- [27] D. Pérez, I. Gasulla, L. Crudgington, D. J. Thomson, A. Z. Khokhar, K. Li, W. Cao, G. Z. Mashanovich, and J. Capmany, “Multipurpose silicon photonics signal processor core,” *Nature Communications*, vol. 8, no. 1, p. 636, 9 2017.
- [28] D. Marpaung, J. Yao, and J. Capmany, “Integrated microwave photonics,” *Nature Photonics*, vol. 13, no. 2, pp. 80–90, 2 2019.
- [29] N. C. Harris, G. R. Steinbrecher, M. Prabhu, Y. Lahini, J. Mower, D. Bunandar, C. Chen, F. N. C. Wong, T. Baehr-Jones, M. Hochberg, S. Lloyd, and D. Englund, “Quantum transport simulations in a programmable nanophotonic processor,” *Nature Photonics*, vol. 11, no. 7, pp. 447–452, 7 2017.
- [30] W. Bogaerts, D. Pérez, J. Capmany, D. A. B. Miller, J. Poon, D. Englund, F. Morichetti, and A. Melloni, “Programmable photonic circuits,” *Nature*, vol. 586, no. 7828, pp. 207–216, 10 2020.
- [31] M. B. On, F. Ashtiani, D. Sanchez-Jacome, D. Perez-Lopez, S. J. B. Yoo, and A. Blanco-Redondo, “Programmable integrated photonics for topological hamiltonians,” *Nature Communications*, vol. 15, no. 1, p. 629, Jan 2024.
- [32] T. Dai, A. Ma, J. Mao, Y. Ao, X. Jia, Y. Zheng, C. Zhai, Y. Yang, Z. Li, B. Tang, J. Luo, B. Zhang, X. Hu, Q. Gong, and J. Wang, “A programmable topological photonic chip,” *Nature Materials*, vol. 23, no. 7, pp. 928–936, Jul 2024.
- [33] A. Ma, T. Dai, J. Mao, Z. Fu, Y. Yang, X. Hu, Q. Gong, and J. Wang, “Anisotropic quantum transport in a programmable photonic topological insulator,” *Optica*, vol. 11, no. 11, pp. 1533–1539, Nov 2024.
- [34] S. Love, M. H. Idjadi, F. Ashtiani, H. H.-W. Lee, and A. Blanco-Redondo, “A programmable platform for photonic topological insulators,” *Nanophotonics*, vol. 14, no. 3, pp. 367–373, 2025.

**Acknowledgments:** A.C., Z.Xu, G.K and A.W.E acknowledge the support from Knut and Alice Wallenberg (KAW) Foundation through the Wallenberg Centre for Quantum Technology (WACQT). J.G. acknowledges support from Swedish Research Council (Ref: 2023-06671 and 2023-05288), Vinnova project (Ref: 2024-00466) and the Göran Gustafsson Foundation. A.W.E acknowledges support from Swedish Research Council (VR) Starting Grant (Ref: 2016-03905). V.Z. acknowledges support from the KAW. I. M. K. acknowledges support by the European Research Council under the European Union’s Seventh Framework Program Synergy ERC-2018-SyG HERO-810451.

**Author contributions:** A.C. performed the experiments, simulations, data analysis, and manuscript drafting. I.K. and A.W.E conceived the idea. A.C., R.Y., and Z.-S.X. developed the experimental platform. G.K. contributed to discussions on the unitary decomposition algorithm and calibration procedure. I.K., J.G., and A.W.E. discussed the results and contributed to the manuscript. A.W.E. and J.G. supervised the project. V.Z. provided input on the manuscript.

**Competing interests:** The authors declare no competing financial interests.

**Data and materials availability:** The authors agree to make any data necessary to support or replicate the claims made in this article available upon reasonable request.